Mechanisms Contributing to Suppressed Precipitation in Mt. Hua of Central China. Part I: Mountain Valley Circulation

YAN YANG

Chinese Academy of Meteorological Sciences, and College of Earth Sciences, University of Chinese Academy of Sciences, Beijing, China, and Atmospheric Sciences and Global Change Division, Pacific Northwest National Laboratory, Richland, Washington

JIWEN FAN, L. RUBY LEUNG, AND CHUN ZHAO

Atmospheric Sciences and Global Change Division, Pacific Northwest National Laboratory, Richland, Washington

ZHANQING LI

State Key Laboratory of Earth Surface Processes and Resource Ecology, and College of Global Change and Earth System Science, Beijing Normal University, Beijing, China, and Earth System Science Interdisciplinary Center, and Department of Atmospheric and Oceanic Science, University of Maryland, College Park, College Park, Maryland

DANIEL ROSENFELD

Institute of Earth Sciences, Hebrew University of Jerusalem, Jerusalem, Israel

(Manuscript received 11 August 2015, in final form 4 December 2015)

ABSTRACT

A significant reduction in precipitation in the past decades has been documented over many mountain ranges such as those in central and eastern China. Consistent with the increase of air pollution in these regions, it has been argued that the precipitation trend is linked to the aerosol microphysical effect on suppressing warm rain. Rigorous quantitative investigations on the reasons responsible for the precipitation reduction are lacking. In this study, an improved Weather Research and Forecasting (WRF) Model with online coupled chemistry (WRF-Chem) is applied and simulations are conducted at the convection-permitting scale to explore the major mechanisms governing changes in precipitation from orographic clouds in the Mt. Hua area in central China. It is found that anthropogenic pollution contributes to a ~40% reduction of precipitation over Mt. Hua during the 1-month summertime period. The reduction is mainly associated with precipitation events associated with valley–mountain circulation and a mesoscale cold-front event. In this paper (Part I), the mechanism leading to a significant reduction for the cases associated with valley–mountain circulation is scrutinized. It is found that the valley breeze is weakened by aerosols as a result of absorbing aerosol-induced warming aloft and cooling near the surface as a result of aerosol–radiation interaction (ARI). The weakened valley breeze and the reduced water vapor in the valley due to reduced evapotranspiration as a result of surface cooling significantly reduce the transport of water vapor from the valley to mountain and the relative humidity over the mountain, thus suppressing convection and precipitation in the mountain.

1. Introduction

Precipitation plays a key role in the hydrological cycle of the earth system. Precipitation over mountain ranges is especially important since it provides the major source of water supply for agriculture and domestic and industrial use. A significant reduction of precipitation has been documented in the past decades over many mountain ranges such as those in the western and eastern United States and central and eastern China (e.g., Givati and Rosenfeld 2004; Rosenfeld et al. 2007; Yang and Gong 2010; Yang et al. 2013a,b). The long-term reduction trend has been attributed to anthropogenic aerosols upwind of the mountains that suppress rain by reducing droplet size that leads to less efficient conversion of droplets to

Corresponding author address: Jiwen Fan, Atmospheric Sciences and Global Change Division, Pacific Northwest National Laboratory, P.O. Box 999, MSIN K9-30, Richland, WA 99352.
E-mail: jiwen.fan@pnnl.gov

DOI: 10.1175/JAS-D-15-0233.1

© 2016 American Meteorological Society

Brought to you by NOAA Central Library | Unauthenticated | Downloaded 08/13/24 01:21 PM UTC

raindrops (e.g., Givati and Rosenfeld 2004; Rosenfeld et al. 2007; Zubler et al. 2011).

Aerosols can alter clouds and precipitation through both aerosol–radiation interaction (ARI) and aerosol–cloud interaction (ACI), which currently constitute the largest uncertainty in climate forcing and projection (IPCC 2013). Through ARI, aerosol particles reduce the energy reaching the surface by scattering and absorbing solar radiation. Absorbing aerosols such as black carbon (BC) can also heat the lower-level atmosphere by absorbing sunlight, which may increase atmospheric stability locally and influence the large-scale circulation, convection, and precipitation (e.g., Fan et al. 2008, 2015; Lau and Kim 2006; Zhang et al. 2009a; Bollasina et al. 2011, 2013; Bond et al. 2013; Grant and van den Heever 2014; Lee et al. 2014). ACI includes all the effects induced by cloud condensation nuclei (CCN) or ice nuclei (IN) (Tao et al. 2012; IPCC 2013). Aerosols can impact precipitation through ACI by 1) producing more cloud droplets of smaller drop size that changes cloud microphysics (Twomey 1977), 2) releasing latent heat as a result of changes in microphysical processes that modulate cloud dynamics (e.g., Wang 2005; Khain et al. 2005; van den Heever et al. 2006; Tao et al. 2007; Rosenfeld et al. 2008; Fan et al. 2012; Altaratz et al. 2014), and 3) changing atmospheric stability through radiation feedback from microphysical changes (Fan et al. 2013; Morrison and Grabowski 2012).

For orographic clouds and precipitation, many past studies suggested that aerosols could reduce precipitation or change the spatial distribution of precipitation through the CCN effect (Lynn et al. 2007; Saleeby et al. 2009; Rosenfeld et al. 2007; Givati and Rosenfeld 2004; Jirak and Cotton 2006; Muhlbauer and Lohmann 2008; Saleeby et al. 2013; Guo et al. 2014; Xiao et al. 2014). Through the IN effect, Fan et al. (2014) and Muhlbauer and Lohmann (2009) found increased precipitation through enhanced snow formation. Enhanced orographic precipitation associated with dust particles that serve as IN to enhance ice formation is supported by observations in the western United States (Ault et al. 2011; Creamean et al. 2013). A majority of past studies on aerosol impacts on orographic precipitation focused on ACI because ARI was not a concern, and also most cases studied previously were wintertime orographic clouds. Absorbing aerosols can significantly change atmospheric stability, convection, and orographic precipitation through ARI (Fan et al. 2015), but such effect has not been investigated as much as the effect of ACI in the past.

Orographic precipitation is highly impacted by air coming from the upwind area (Levin and Cotton 2009), which is usually a low-elevation plain with severe air pollution in many locations of China (Guo et al. 2014; Yang and Gong 2010). A few observational studies found decreasing trends of orographic precipitation that correlate well with the increased air pollution in central and eastern China (e.g., Rosenfeld et al. 2007; Yang and Gong 2010; Yang et al. 2013a,b; Guo et al. 2014). Different reasons are speculated to explain the decreasing trend of orographic precipitation: Rosenfeld et al. (2007) linked the reduced precipitation at Mt. Hua with microphysical aerosol effect on suppressing rain; Yang and Gong (2010) hypothesized that reduction of wind speed might suppress rainfall in the mountain areas in eastern China by weakening the orographic lifting. Yang et al. (2013a,b) performed further observational analysis at Mt. Hua and corroborated the decreasing trend of precipitation revealed by Rosenfeld et al. (2007) with many more meteorological variables analyzed and further insights gained. They hinted that wind speed changes from aerosol radiative effect may alter the energy transport and further contribute to the precipitation change. Aerosols in the surrounding plain area such as Xi'an are strongly light absorbing (Lee et al. 2007), and the impact of the highly absorbing aerosols on mountain precipitation is not clear yet.

It is worth noting that these arguments are largely hypothetical and have yet to be rigorously investigated and quantified by model simulations because available measurements to pinpoint the exact mechanisms are very limited. The major factors leading to the decreasing trends of orographic precipitation may vary with locations, cloud dynamics, and other environmental conditions. Given the relatively large number of observation-based studies conducted in the Mt. Hua area (Rosenfeld et al. 2007; Yang et al. 2013a,b), we have conducted model simulations to investigate the major mechanisms contributing to the suppression of precipitation that was concluded unanimously by those observational studies. The modeling study is carried out on the convection-permitting scale over a large regional domain in central China by real-case simulations with coupled chemistry and aerosols to explore the major mechanisms responsible for the reduced precipitation over the Mt. Hua area.

2. Methods

Model simulations are conducted using the improved Weather Research and Forecasting (WRF) Model with online coupled chemistry, version 3.4.1 (WRF-Chem v3.4.1), with the Model for Simulating Aerosol Interactions and Chemistry (MOSAIC) (Zaveri et al. 2008) and Carbon Bond Mechanism (CBMZ) photochemical mechanism (Zaveri and Peters 1999). The

Brought to you by NOAA Central Library | Unauthenticated | Downloaded 08/13/24 01:21 PM UTC

TABLE 1. Summary of chemistry/aerosol conditions in all simulated cases.

Cases	Emissions	Chemistry/aerosol boundary conditions	Chemistry/aerosol initial conditions[a]	Aerosol–radiation interaction
P_ALL	Present-day emissions in 2006	Global WRF-Chem simulation in 2010	Default profiles in WRF-Chem	Yes
C_ALL	Based on P_ALL, multiplied by 0.33	Based on P_ALL, multiplied by 0.33	Same as P_ALL	Yes
P_NORAD	Same as P_ALL	Same as P_ALL	Same as P_ALL	No
C_NORAD	Same as C_ALL	Same as C_ALL	Same as P_ALL	No

[a] Chemistry/aerosol initial values are the default profiles in WRF-Chem, which are small. It does not matter in our simulation since emissions control quickly. Also all simulations have at least 7 days of spinup.

MOSAIC aerosol scheme uses the sectional approach to represent aerosol size distributions with a number of discrete size bins (four bins in this study) (Fast et al. 2006). All major aerosol components including sulfate (SO_4^{2-}), nitrate (NO_3^-), ammonium (NH_4^+), BC, organic matter (OM), sea salt, and mineral dust are simulated in the model. Aerosol optical properties such as extinction, single-scattering albedo, and asymmetry factor for scattering are computed as a function of wavelength at each model grid box. Aerosol–radiation interaction is coupled with the Rapid Radiative Transfer Model (RRTM) with GCM applications (RRTMG) (Iacono et al. 2008) for both shortwave (SW) and longwave radiation as implemented by Zhao et al. (2013a).

Anthropogenic emissions are obtained from the Asian emission inventory described by Zhang et al. (2009b) at 0.5° × 0.5° horizontal resolution for 2006. Biomass burning emissions are obtained from the Global Fire Emissions Database, version 3 (GFEDv3), with a monthly temporal resolution, a 0.5° × 0.5° horizontal resolution (van der Werf et al. 2010), and a vertical distribution following the injection heights suggested by Dentener et al. (2006) for the Aerosol Comparisons between Observations and Models (AeroCom) project. Dust emissions follow Zhao et al. (2010), with vertical dust fluxes calculated with the Goddard Chemistry Aerosol Radiation and Transport (GOCART) dust emission scheme (Ginoux et al. 2001). The emitted dust particles are distributed into the MOSAIC aerosol size bins following a theoretical expression based on the physics of scale-invariant fragmentation of brittle materials derived by Kok (2011). The main aerosol compositions over the region are sulfate and black carbon from anthropogenic emissions. Biomass burning and dust are not significant emission sources.

The simulation using emissions described above is named P_ALL, the base case simulation (Table 1). To investigate the effects of anthropogenic emissions, a sensitivity test is carried out based on P_ALL, but with anthropogenic emissions scaled by a factor of 0.3

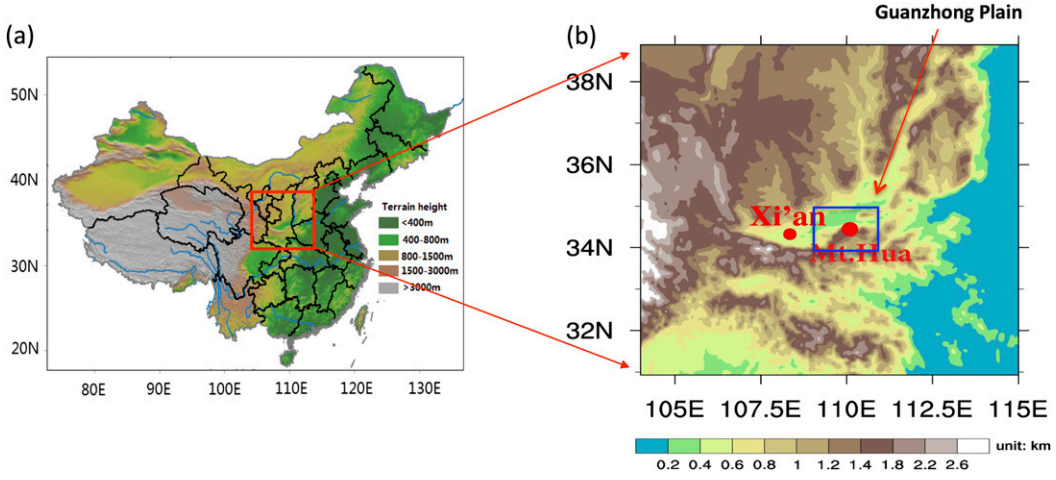

FIG. 1. (a) Map of China with terrain height. The red box is the simulation domain (31°–39°N, 104°–115°E). (b) The enlarged simulation domain with detailed topography. The locations of Mt. Hua and Xi'an are marked. The blue box in (b) is the study domain.

Brought to you by NOAA Central Library | Unauthenticated | Downloaded 08/13/24 01:21 PM UTC

TABLE 2. Physical and chemical parameterizations employed in the simulations.

Types	Schemes
Planetary boundary layer	YSU planetary boundary layer scheme
Land surface model	Unified Noah land surface scheme
Shortwave radiation	RRTMG
Longwave radiation	RRTMG
Microphysics	Morrison two-moment scheme
Chemistry	CBMZ
Aerosol	MOSAIC 4 bins

(referred to as "C_ALL"). The factor was obtained based on the approximate ratio of the SO_2 emissions in the early 1980s in China before the economic development to the current emissions (Bennartz et al. 2011). To explore the contributions of ARI and ACI, respectively, simulations named P_NORAD and C_NORAD are conducted by turning off ARI based on the same configuration of P_ALL and C_ALL, respectively. The precipitation and convective intensity of C_NORAD is very similar to C_ALL since ARI is small under the clean environment, so only C_ALL is included in most of the results presented.

The simulation is performed at $3 \times 3\,km^2$ horizontal resolution with 420×420 grid cells (31°–39°N, 104°–115°E) and 40 vertical layers up to 50 hPa. The model domain covers a large part of central China (Fig. 1a) and is centered at Guanzhong Plain as shown in Fig. 1b. The meteorological initial and lateral boundary conditions are derived from the National Centers for Environmental Prediction Final Analysis (NCEP FNL) data at 1° horizontal resolution and 6-h temporal intervals.

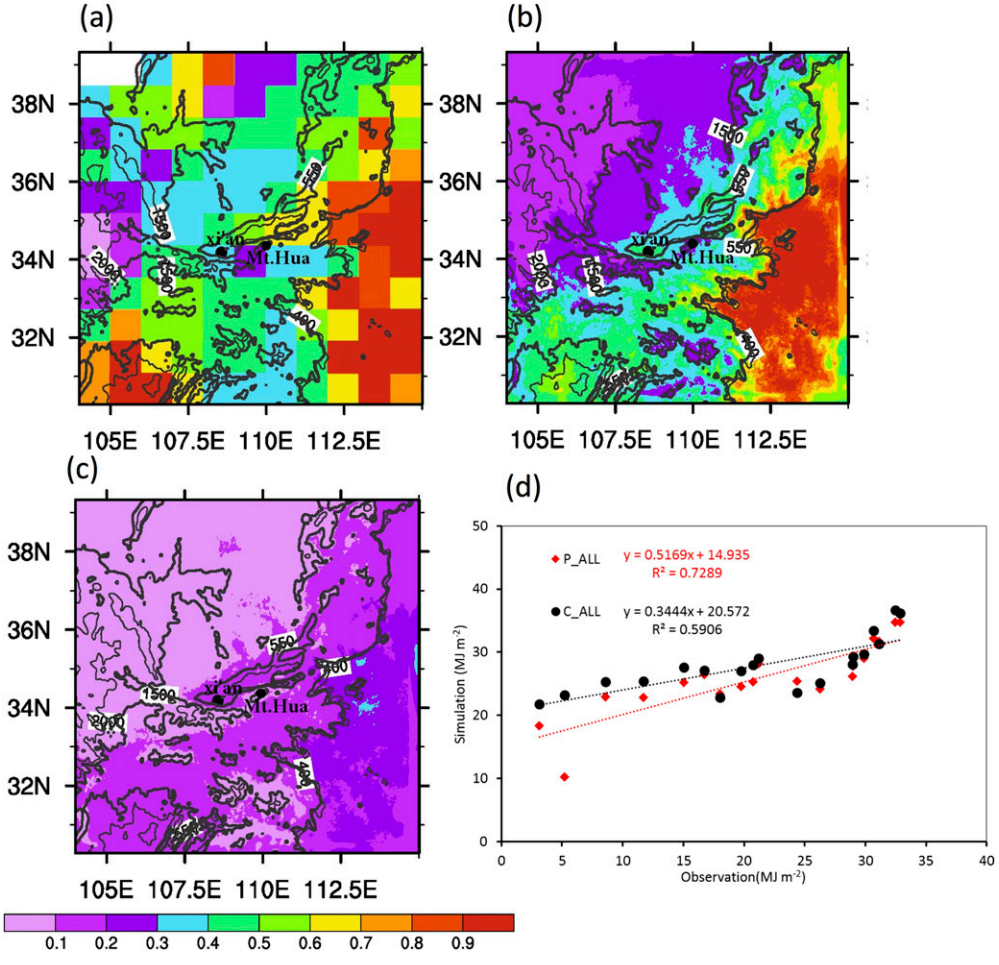

FIG. 2. Spatial distribution of clear-sky AOD at 550-nm wavelength averaged over the study time period (1–20 Jul 2008) from (a) the satellite observations, (b) P_ALL, and (c) C_ALL. (d) The correlations of daily accumulated surface shortwave radiative fluxes measured at Jinghe (34°26′N, 108°58′E), ~30 km west of Xi'an, with those in P_ALL and C_ALL. The data points shown are the summed surface shortwave radiative fluxes over each study day; at the time of writing, the data were available at http://www.nmic.gov.cn/web/channel-8.htm. The observed 550-nm AOD was obtained from http://ladsweb.nascom.nasa.gov/data/.

Brought to you by NOAA Central Library | Unauthenticated | Downloaded 08/13/24 01:21 PM UTC

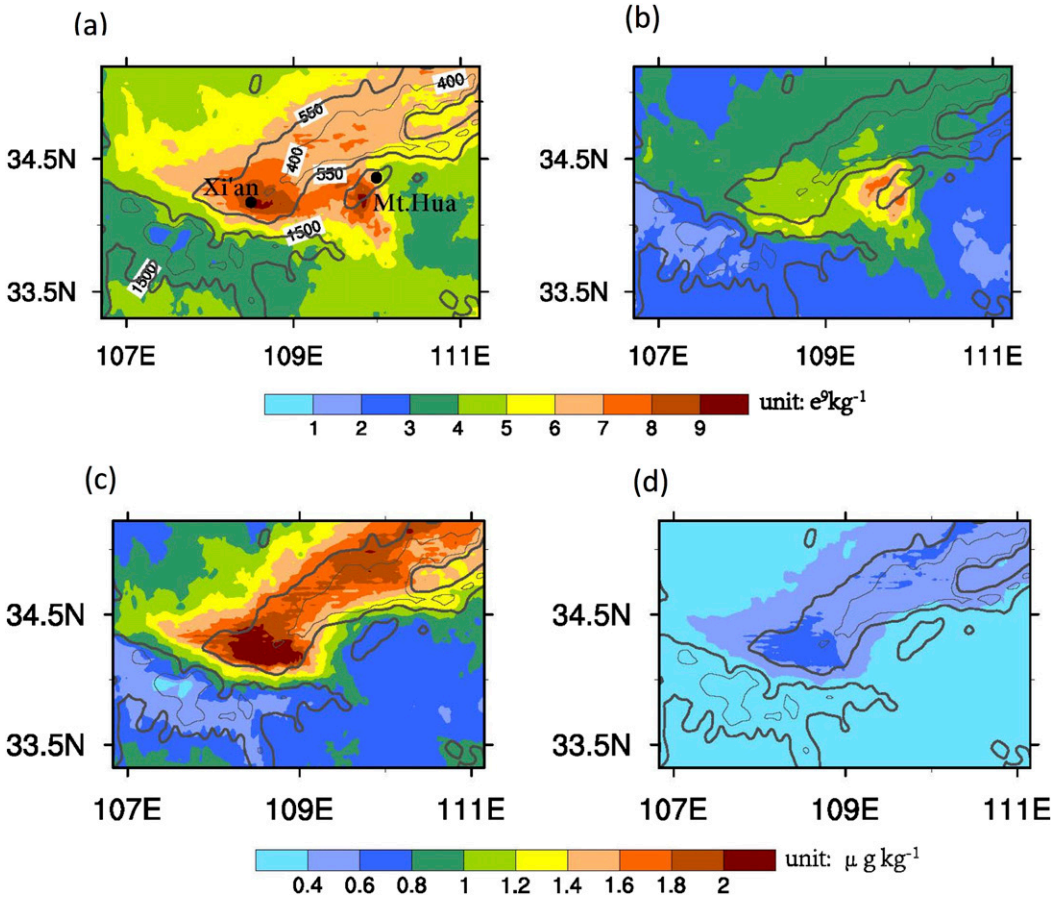

FIG. 3. Aerosol number mixing ratios from (a) P_ALL and (b) C_ALL at the 500-m height above the surface. (c),(d) The corresponding BC mass mixing ratios. The gray contours denote the terrain heights of 400, 550 (boldface), and 1500 m (boldface).

Nesting is not used to avoid the gray zone problems for cumulus parameterizations (Liu et al. 2015; Arakawa and Wu 2013), so to reduce dynamical shocks near the lateral boundaries transitioning from 1° to 3-km resolution, a large buffering zone is set with 15 grid points at the lateral boundaries. The chemical initial condition is from the default profiles provided by WRF-Chem, which corresponds to a very clean condition, while the chemical boundary condition is provided by a quasi-global WRF-Chem simulation (Zhao et al. 2013b). The Yonsei University (YSU) planetary boundary layer scheme (Hong et al. 2006), Unified Noah land surface scheme (Chen and Dudhia 2001), Morrison two-moment microphysics scheme (Morrison et al. 2005), and RRTMG longwave and shortwave radiation schemes (Iacono et al. 2008) are used in this study. At the 3-km convection-permitting scale, cumulus cloud parameterization is not needed. The model setup and physical schemes are shown in Table 2.

The simulations described in Table 1 are run for 27 days during the summer of 2008, starting from 0000 UTC 23 June and ending at 2300 UTC 20 July. Only the data from 0000 UTC 1 July to 2300 UTC 20 July are included in the analysis to allow 7 days of model spinup. We study aerosol effects in the summertime when there are more convective clouds and precipitation associated with the East Asian summer monsoon that influences the study region.

3. Results and discussion

The P_ALL simulation with the current emissions captures the aerosol optical depth (AOD) values in agreement with the MODIS measurements, especially at the Guanzhong Plain where Xi'an is located and in the Mt. Hua region where this study focuses (Fig. 2b vs 2a). The underestimation of AOD around the top- and bottom-left corners of the domain would not affect the Guanzhong Plain and Mt. Hua regions since they are not located upwind and are far away from the study area. The AOD at the Guanzhong Plain is ~0.5, which is not

Brought to you by NOAA Central Library | Unauthenticated | Downloaded 08/13/24 01:21 PM UTC

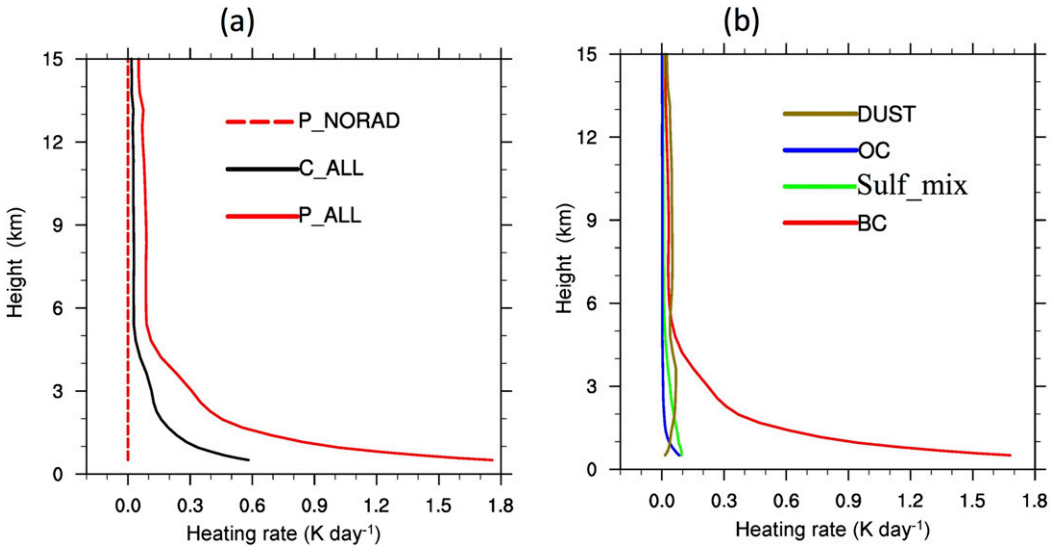

FIG. 4. Vertical profiles of (a) total aerosol heating rates from P_ALL, C_ALL, and P_NORAD and (b) the respective heating rates from sulfate and its mixture (sulf_mix), dust, OC, and BC in P_ALL. The heating rate is calculated for clear-sky grid points (total water condensate of $<10^{-6}$ kg kg^{-1}) and averaged over the Guanzhong Plain (i.e., terrain height >550 m over 34°–34.5°N, 108.5°–109.5°E).

very high (Fig. 2a). However, the corresponding aerosol number concentrations N_a are very high ($>8 \times 10^9$ kg^{-1} at 500-m height above the surface) (Fig. 3a) with a large amount of BC (Fig. 3c) and large aerosol heating rates (up to 1.8 K day^{-1}) as a result of BC heating (Fig. 4b). In contrast, in the southeast of the domain, we see very high AOD (>0.8) but N_a is much lower than that of the Guanzhong Plain. Note that the relationship between AOD and N_a is determined by aerosol composition and mixing states and air humidity, suggesting very different environmental conditions and aerosol sources in the Guanzhong Plain compared to the areas in the southeast of the domain. It is also noted that, in the Mt. Hua area, there is a high aerosol number mixing ratio but AOD is low (Figs. 2 and 3). Xi'an is located upwind of Mt. Hua during daytime and the aerosol number mixing ratio is always high at Xi'an. But the aerosol number mixing ratio over Mt. Hua is low in the morning and increases gradually throughout the day. The high aerosol number mixing ratio in Mt. Hua seems to be associated with the transport of aerosols by the prevailing wind from the Guanzhong Plain where Xi'an resides. Aerosols that survive the long-distance transport are generally small and/or have low hygroscopicity, so they do not contribute much to AOD, explaining the low AOD there. The very low heating rate of organic carbon (OC) and the stronger heating rate of sulfate compared to OC shown in Fig. 4b are likely because 1) OC emissions are at a minimum in July (Zhang et al. 2009b) and 2) the heating rate includes sulfate mixing with other compounds such as BC.

We further compare surface radiative fluxes (daily accumulated shortwave radiation) measured at Jinghe, which is about 30 km west of Xi'an (Fig. 2d) with the modeled results as shown in Fig. 2d. During the study period, surface shortwave radiative flux simulated for P_ALL agrees well with observations with a correlation coefficient of 0.73, significantly better than C_ALL with a correlation coefficient of 0.59.

P_ALL simulates the average daily precipitation well compared with rain gauge data from stations shown in Fig. 5a with a correlation coefficient of 0.45 (Fig. 5b). The correlation coefficient between C_ALL and observations is only 0.21, and the precipitation rates at most of the stations are largely overestimated. Although P_ALL slightly overestimates the rain-rate frequency across all rain categories, it agrees with observations much better compared with the clean case (C_ALL) that evidently overestimates rain-rate frequency by 100% generally (Fig. 5c). Note that both N_a and aerosol heating rate in P_ALL are about 3 times larger than those of C_ALL as shown in Figs. 3 and 4. Therefore, C_ALL represents a much cleaner condition relative to P_ALL, though it might still be more polluted than many places in the United States and Europe.

Figure 5c shows a significant reduction of the occurrence frequency of all precipitation categories over the large area. Around the Mt. Hua region, there is a 2–6-mm reduction of daily precipitation (~40% reduction on average) in P_ALL compared with C_ALL (marked by a black circle in Fig. 5d). This is consistent with the long-term decreasing trend of precipitation with the

Brought to you by NOAA Central Library | Unauthenticated | Downloaded 08/13/24 01:21 PM UTC

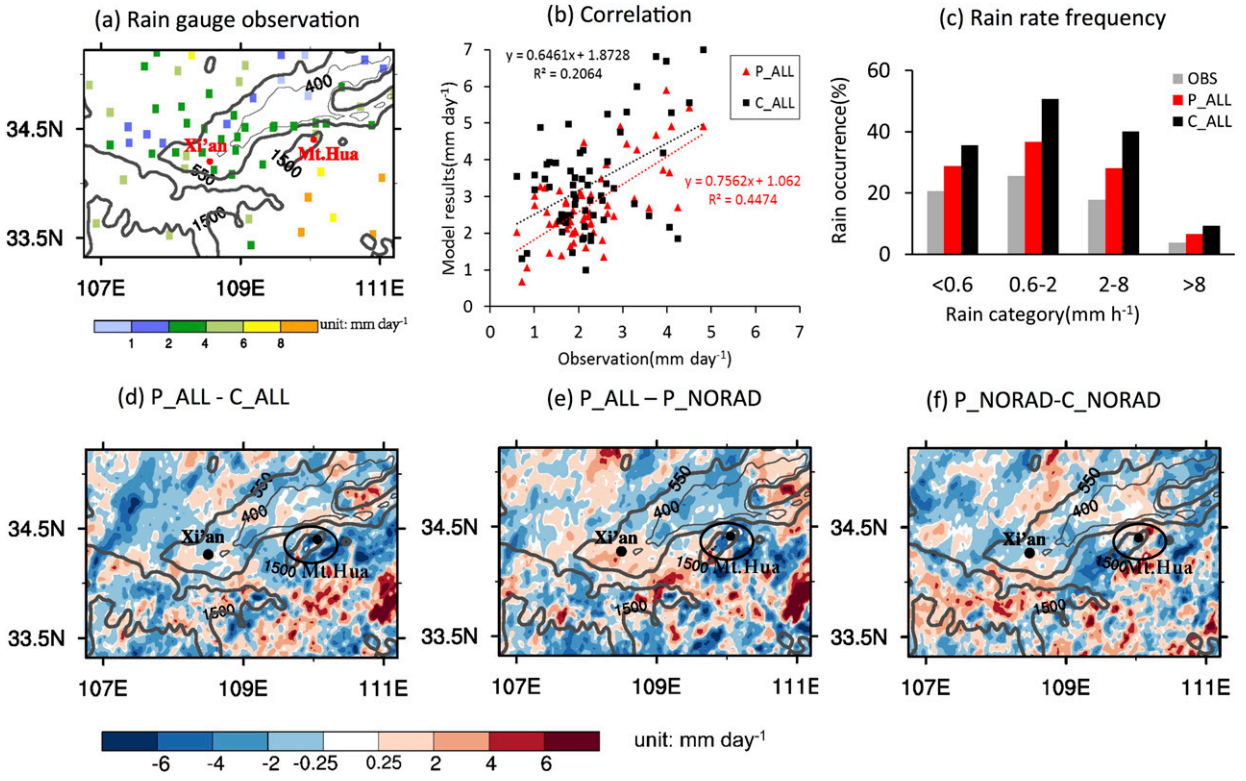

FIG. 5. (a) The average daily precipitation from observed rain gauge stations. (b) The scatterplot of daily mean precipitation showing the correlation of observations from the stations shown in (a) with P_ALL (red) and C_ALL (black). (c) The occurrence frequency of each rain category from observations (gray), P_ALL (red), and C_ALL (black). The data considered are the hourly precipitation rates with a rain rate > 0.25 mm h^{-1} during the study time period from all the stations as shown in (a) and (b). The modeled data are obtained from the corresponding grid points of the observed stations. For the average daily precipitation, (d) P_ALL − C_ALL, (e) P_ALL − P_NORAD, and (f) P_NORAD − C_NORAD. The gray contours are the terrain heights of 400, 550 (boldface), and 1500 m (boldface). The black circle in (d)–(f) marks the Mt. Hua area that we focus on in this study.

decrease of visibility in the recent decades observed at stations in Mt. Hua as revealed by Rosenfeld et al. (2007) and Yang et al. (2013a). In the Xi'an region, however, the precipitation changes are not evident and the sign can be either positive or negative (Fig. 5d). Therefore, we focus on elucidating the significant reduction of precipitation at the Mt. Hua region, which is corroborated by observations as discussed above and also shown in Fig. 6e.

A similar amount of reduction of precipitation in the Mt. Hua area is seen between P_ALL, which considers both ARI and ACI, and P_NORAD in which only ACI is considered (Fig. 5e), suggesting that ARI is the main contributor to the reduction of precipitation in Mt. Hua. This is further attested by the differences of precipitation between P_NORAD and C_NORAD (Fig. 5f), which shows that ACI only slightly enhances precipitation over the Mt. Hua area. Therefore, our modeling results suggest that ACI has a small contribution to the "observed" reduction of precipitation in the Mt. Hua area. However, we note that ACI is simulated using the Morrison two-moment microphysics scheme, which may have limitation for representing aerosol indirect effects (Wang et al. 2013; Milbrandt and Yau 2005). Nevertheless, in a heavily polluted environment especially with strong absorbing aerosols, ARI has been shown to be dominant in the theoretical calculations of Rosenfeld et al. (2008) and a modeling study using a bin cloud model (Fan et al. 2008). This study further supports that ARI is dominant in environments with highly absorbing aerosols that are common in South and East Asia. Therefore, uncertainty in modeling ACI should not impact the main findings of this study. It should be noted that it is a challenge in computational cost to conduct similar model simulations using bin cloud microphysics with chemistry over such a large domain for a long time period (~1 month).

To examine how ARI leads to the reduction of precipitation for the summer convective clouds over the Mt. Hua area, we analyze the precipitation for daytime and

Brought to you by NOAA Central Library | Unauthenticated | Downloaded 08/13/24 01:21 PM UTC

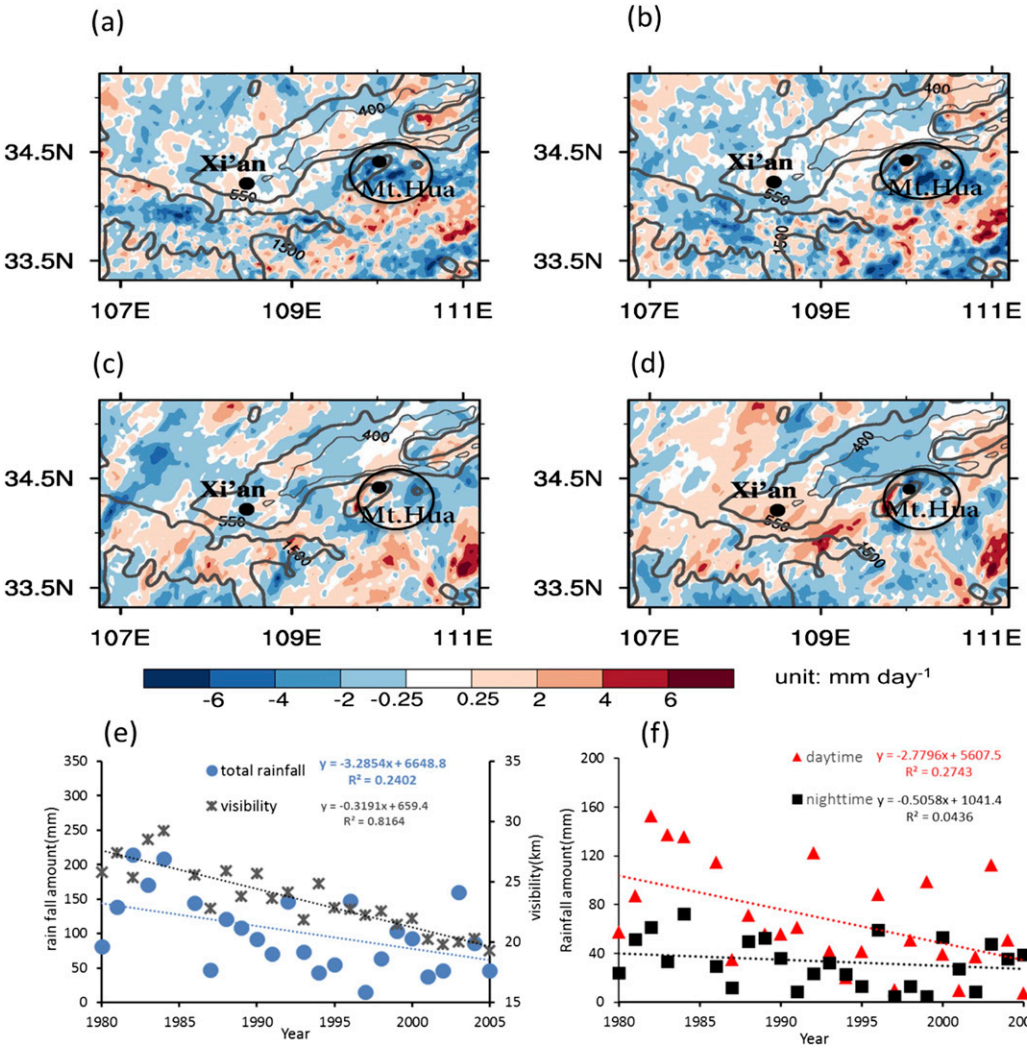

FIG. 6. For the average daytime precipitation, (a) P_ALL − C_ALL and (b) P_ALL − P_NORAD during the study time period. (c),(d) As in (a),(b), but for nighttime. (e) The long-term precipitation and visibility trends in Mt. Hua in July and (f) the separated precipitation trends for daytime (red) and nighttime (black) based on (e). The precipitation amount for each year in (e),(f) is the total precipitation summed over the month of July based on 6-hourly data collected at the Mt. Hua observatory station (34°48′N, 110°08′E). The visibility is averaged over the month of July based on four observations per day at the Mt. Hua observatory station and has been converted to the equivalent visibility in dry conditions as mentioned in Rosenfeld et al. (2007). The data for July 1985 have been removed because of an extreme precipitation event on 10 Jul 1985. The observation data are from the global surface weather dataset from the China National Meteorological Information Center (at the time of writing, the data were available at http://www.nmic.gov.cn/web/channel-8.htm). The gray contours in (a)–(d) are the terrain heights of 400, 550 (boldface), and 1500 m (boldface).

nighttime, respectively, given that ARI is produced only in daytime and the local circulation between the valley and mountain usually has distinct differences between daytime and nighttime. Daytime is defined as 0800–2000 local standard time (LST) based on positive surface shortwave radiation. To facilitate the discussion of diurnal processes, all the times shown in this paper are in LST. As shown in Fig. 6, the reduction of precipitation in the Mt. Hua area (black circle) mainly occurs during daytime (Figs. 6a,b), while at night, the reduction is marginal and a slight increase is seen in some locations of the area (Figs. 6c,d). The decreasing precipitation in the daytime is consistent with what our model reveals that ARI is the main contributor to the precipitation suppression, as ARI is produced in the daytime through scattering or absorption of solar radiation. The result is also consistent with the long-term observations in Mt. Hua showing the significant decreasing trend of precipitation in the daytime but not much change in the nighttime (Fig. 6f).

Brought to you by NOAA Central Library | Unauthenticated | Downloaded 08/13/24 01:21 PM UTC

To scrutinize the mechanism for ARI to reduce precipitation during the 20-day analysis time period, similar precipitation events are composited to reveal the common characteristics. The simulations reveal three convective categories for the days when daytime precipitation is significant. Category 1 represents the typical afternoon storm precipitation in Mt Hua that is mainly associated with valley–mountain circulation. This category includes precipitation events on 1, 2, 7, 8, 9, 10, 12, 19, and 20 July and accounts for 41% of the total daytime precipitation in the polluted case (P_ALL) over the analysis time period. Category 2 has a late morning precipitation peak and also an afternoon peak. Although this category only occurred on 4 July, it contributes 43% to the total daytime precipitation in P_ALL. Category 3 represents the cases with very early morning precipitation (i.e., 13, 14, 15, and 17 July), which is usually a continuation of a precipitation event from the previous night. This category contributes only about 16% to the total daytime precipitation in P_ALL. Since the daytime precipitation from the clean to polluted cases does not change significantly for category 3 (Fig. 7c), it is excluded from the following analysis. The decreased precipitation in very early morning from C_ALL (or P_NORAD) to P_ALL can be contributed by ACI that suppresses warm rain by increasing cloud droplet number concentrations but reducing droplet sizes. As the overall contribution of this effect is very small, our focus will be on categories 1 and 2.

Category 2 only includes one convective system on 4 July, which is a mesoscale cold-front system forming an extratropical cyclone in the front pocket of the westerly trough. The dramatic reduction (5 times more; Fig. 7b) of precipitation from C_ALL (or P_NORAD) to P_ALL in the Mt. Hua area is associated with changes of the circulation pattern, which will be presented in the forthcoming Part II of the research. Therefore, the remaining part of this paper focuses on how ARI leads to the reduction of precipitation for the category-1 cases (Fig. 7a), in which ARI suppresses the daytime averaged precipitation by 30%.

For category 1, precipitation mostly occurs in the afternoon. A typical valley breeze develops during daytime and a mountain breeze is seen during nighttime in the analysis period (Figs. 8a,b). Valley and mountain breezes form through a process similar to sea and land breezes. During the day, solar absorption near the surface of the mountain heats the air more rapidly than air at the same altitude above the valley. Because of this differential heating, a valley breeze develops and converges in the mountain. At night, the process is reversed because heat loss from the surface of the mountain cools the air more rapidly than air above the valley and a nocturnal downslope wind develops that blows from the mountain toward the valley. To explain the daytime precipitation reduction by aerosols, valley breeze will be further analyzed.

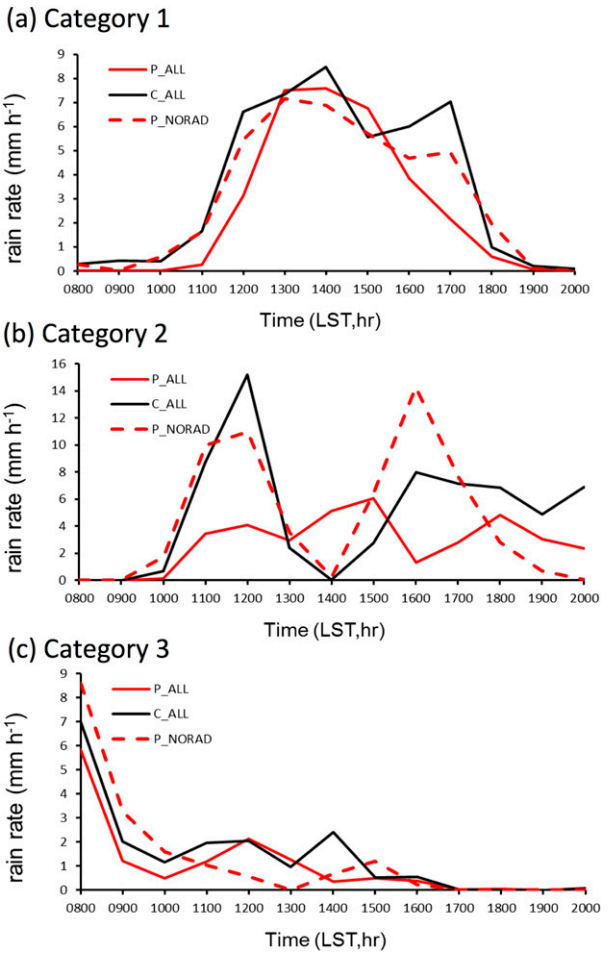

FIG. 7. Rain rates during daytime averaged over the Mt. Hua area as marked by the blue box in Fig. 1b for P_ALL, C_ALL, and P_NORAD for categories (a) 1, (b) 2, and (c) 3.

We first examine the changes of convective intensity between the polluted and clean cases for category 1. As shown in Fig. 8c, convection over the mountaintop area is evidently suppressed in P_ALL compared with those of C_ALL and P_NORAD, especially for the strong convection. The maximum updraft velocity averaged over the daytime period of all the cases in category 1 over the mountaintop area is 5.3 m s^{-1} in P_ALL compared to 5.8 m s^{-1} in C_ALL. The corresponding value for P_NORAD is 5.9 m s^{-1} (Fig. 8d). These results suggest that ARI in P_ALL leads to weakened convection over the mountain. As a result of weakened convection, the ice-related processes are suppressed and therefore we see significantly reduced ice-precipitating particles (i.e., snow and graupel) in mass mixing ratios from C_ALL (or P_NORAD) to P_ALL (Table 3) and, therefore, the reduced surface precipitation.

Brought to you by NOAA Central Library | Unauthenticated | Downloaded 08/13/24 01:21 PM UTC

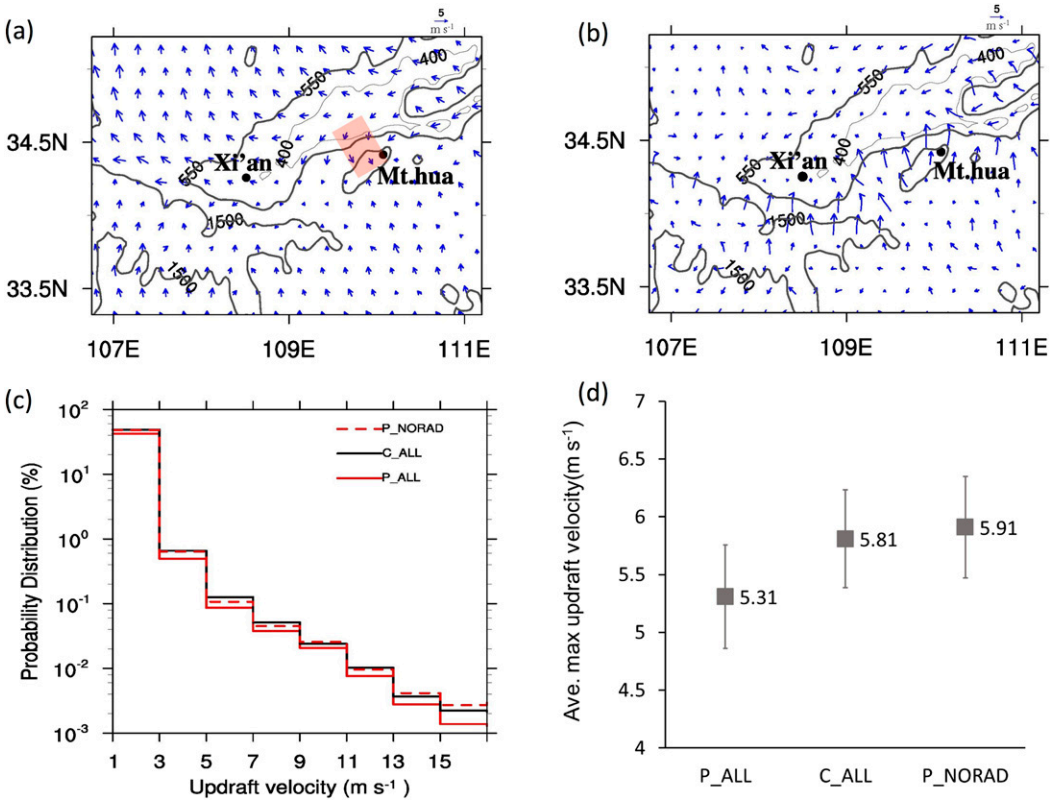

FIG. 8. Wind field at 10 m averaged over (a) 1200–1400 and (b) 2300–0100 LST from P_ALL. (c) PDF of updraft velocity during daytime over the Mt. Hua area from C_ALL (black solid), P_ALL (red solid), and P_NORAD (red dashed). (d) The max vertical velocity averaged over the daytime based on the hourly outputs from the three simulations at the Mt. Hua top area. Here, the Mt. Hua top area is identified for the grid points with a terrain height of larger than 1500 m in the domain marked by the blue box in Fig. 1b (i.e., near the mountaintop area). The shaded rectangle marked in (a) shows the cross sections used for plotting Fig. 9. Plots are for cases of category 1.

A significant weakened valley breeze circulation induced by ARI is found for category-1 cases, which can contribute significantly to the weakened convection. Along the wind blowing from the valley to mountain, the cross section figures are plotted to more clearly show the changes of valley breeze by ARI from C_ALL to P_ALL (Figs. 9a–d). To obtain more representative results, some quantities as shown in Fig. 10 are plotted over the same area as in Figs. 8c and 8d, instead of over the cross sections. Under the clear-sky conditions, aerosols result in a heating layer aloft (at 1.3–3.0-km altitude in the plain) (Figs. 9a,b). The largest warming is at the altitudes of 1.6–2.2 km (Fig. 9b) (i.e., at similar altitudes of the mountaintop area), leading to a significantly reduced temperature difference between the mountain and plain at these altitudes during 1100–1400 LST in the polluted case compared to the clean case or the polluted case without ARI, with the largest decrease

TABLE 3. Cloud hydrometer number and mass mixing ratios averaged over the same mountaintop area and over the daytime period (0800–2000 LST) as in Fig. 8c for category-1 cases.

	Droplet	Raindrop	Cloud ice	Snow	Graupel
Number (kg^{-1})					
P_ALL	2.32×10^{7}	2.38×10^{2}	4.20×10^{3}	2.90×10^{2}	2.54×10^{2}
C_ALL	1.63×10^{7}	5.04×10^{2}	3.65×10^{3}	1.99×10^{2}	1.37×10^{2}
P_NORAD	2.24×10^{7}	3.63×10^{2}	3.96×10^{3}	3.21×10^{2}	2.82×10^{2}
Mass ($g\,kg^{-1}$)					
P_ALL	8.37×10^{-3}	5.01×10^{-3}	9.86×10^{-4}	3.44×10^{-3}	0.92×10^{-2}
C_ALL	7.43×10^{-3}	7.86×10^{-3}	5.95×10^{-4}	4.39×10^{-3}	1.03×10^{-2}
P_NORAD	8.98×10^{-3}	5.94×10^{-3}	8.80×10^{-4}	4.66×10^{-3}	1.68×10^{-2}

Brought to you by NOAA Central Library | Unauthenticated | Downloaded 08/13/24 01:21 PM UTC

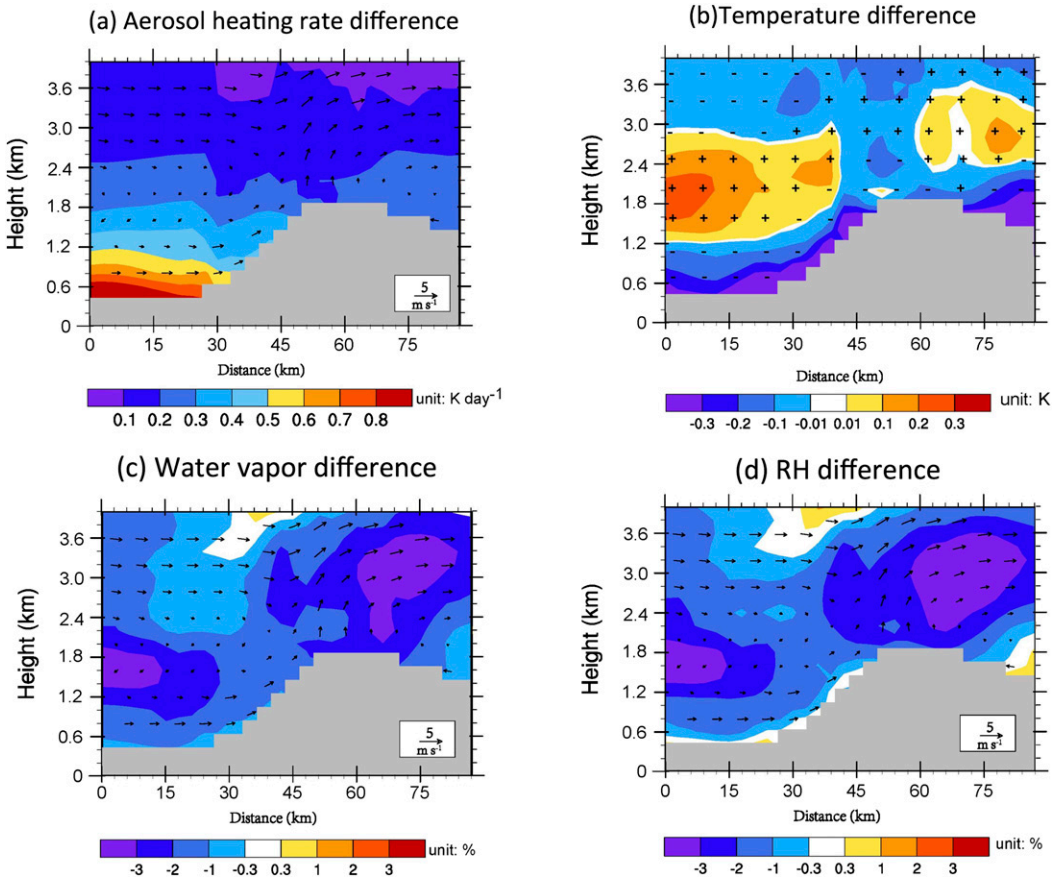

FIG. 9. The differences of clear-sky (a) aerosol heating rate, (b) temperature, (c) water vapor, and (d) RH between P_ALL and C_ALL averaged over the daytime period (i.e., 0800–2000 LST) along the cross sections, which are chosen along the wind direction from the valley to Mt. Hua as shown by the shaded rectangle marked in Fig. 8a with a width of 20 grid points. The arrows in (a),(c), and (d) are the wind simulated in P_ALL within 1200–1400 LST to show the direction of transport. The plus signs and minus signs in (b) denote locations with increased and reduced wind speed between P_ALL and C_ALL, respectively. The clear-sky grid points are defined with the total condensates of less than 10^{-6} kg kg^{-1}. Plots are for cases of category 1.

of ~0.6°C on average at 1200 LST (Fig. 10a). Furthermore, aerosols also cause a strong surface cooling in the valley (Fig. 9b), which suppresses rising motion in the valley. Therefore, both the reduced temperature difference between the plain and mountain at the higher altitudes and the surface cooling in the valley contribute to an evidently weakened valley breeze under the polluted condition through ARI. The valley breeze wind speeds over the hilly area (defined as the grid points with terrain height between 550 and 1500 m in the blue box domain shown in Fig. 1b) are reduced by ~0.7 m s^{-1} (~18%) from C_ALL (or P_NORAD) to P_ALL at 1300 LST averaged over all cases in category 1 (Fig. 10b), which is statistically significant. As a result, the water vapor transport from the plain to Mt. Hua is much reduced and the water vapor at the mountaintop area is evidently reduced by 3%–4% on average (Figs. 9c and 10d). Although temperature at the mountaintop area is slightly reduced (Fig. 9b), which is also associated with aerosol cooling on the mountain surface, the reduction in water vapor dominates over the small cooling, leading to an evident reduction of relative humidity (RH) (Fig. 9d). Therefore, the much dryer condition along with the reduced surface temperature over the mountaintop area inevitably suppresses convection and precipitation.

It is noticed that there is a significant reduction of water vapor at the altitudes of 1.2–2 km in the valley and the water vapor near the surface of the plain is also reduced from the clean to polluted case (Fig. 9c). Based on the circulation shown as the black arrows in Fig. 9c, the water vapor at the altitudes of 1.2–2 km is not strongly transported to anywhere in the daytime owing to the very low wind speeds. Therefore, the reduction of water vapor there would not significantly contribute to the reduction of water vapor over the mountaintop area. The water vapor near the surface in the plain contributes

Brought to you by NOAA Central Library | Unauthenticated | Downloaded 08/13/24 01:21 PM UTC

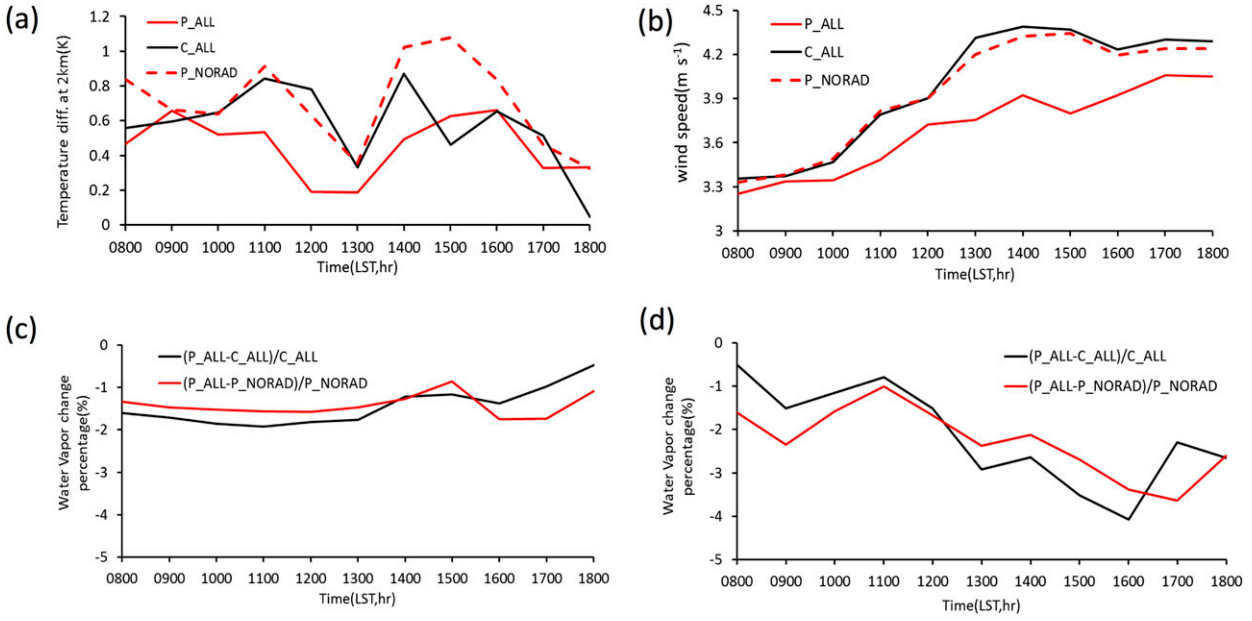

FIG. 10. (a) The temperature differences between the Mt. Hua top area and the plain area at 2-km altitude in P_ALL (red solid), C_ALL (black solid), and P_NORAD (red dashed) during the daytime. (b) The 10-m wind speed in P_ALL (red solid), C_ALL (black solid), and P_NORAD (red dashed) for the upwind hilly area. Water vapor mixing ratio differences (%) averaged over the 0–1-km height above the surface between P_ALL and C_ALL (black) and P_ALL and P_NORAD (red) at the (c) plain and (d) Mt. Hua top area. See the caption of Fig. 8 for the definition of the Mt. Hua top area. The grid points with a terrain height smaller than 550 m in the blue box domain shown in Fig. 1b are defined as the plain area. The upwind hilly area is defined for the grid points with topography between 550 and 1500 m. Plots are for cases of category 1.

directly to that over the mountain owing to moisture transport by the valley breeze. The reduction near the surface of the plain is only about 1% (Figs. 9c and 10c), while the reduction is a couple of times larger over the mountaintop area (Figs. 9c and 10d), suggesting the significant contribution of the weakened valley breeze to the large reduction of the moisture over the mountaintop area. Since the moisture over the mountaintop area at the times before valley breeze is effective (1100 LST) is reduced as well (Fig. 10d) and the reduction is at a similar magnitude as that near the surface of the plain (Fig. 10c), the reduced moisture near the surface of the plain enhances the reduction of the water vapor over the mountain top. The small reduction of water vapor in the planetary boundary layer (PBL) in the plain is contributed by the reduced latent heat flux (LH; about 5%–10%), which is mainly caused by the reduced net surface solar heating and hence less evapotranspiration due to ARI from C_ALL (or P_NORAD) to P_ALL (the black solid line in Fig. 11 denotes the differences between P_ALL and C_ALL and the red solid line is for the differences between P_ALL and P_NORAD). Over the mountaintop area, the reduction of LH and sensible heat flux (SH) is significantly smaller compared with that in the valley (dotted lines of Fig. 11) because aerosol concentration is much lower in the mountain, suggesting its small role in contributing to the moisture reduction.

Figure 12 schematically summarizes the mechanism leading to the reduced mountain precipitation due to ARI for precipitation events driven by valley–mountain circulation; that is, the strong absorbing properties of aerosols in the valley reduce the temperature differences between the valley and mountain at the elevated altitudes and cool the valley surface evidently, both leading to a weakened valley breeze in the daytime, a major mechanism responsible for the reduced water vapor over the mountaintop area. In addition to the weakened valley breeze, the reduced water vapor near the surface of the valley due to reduced evapotranspiration as a result of surface cooling contributes to the further reduction. The dramatically reduced water vapor and RH over the mountain result in much weakened convection and reduced precipitation by suppressing convection intensity and therefore the ice-precipitating hydrometeor production.

4. Conclusions

We have conducted model simulations of clouds and precipitation in the Mt. Hua region at the convection-permitting scale (3 km) for about 1 month during the

Brought to you by NOAA Central Library | Unauthenticated | Downloaded 08/13/24 01:21 PM UTC

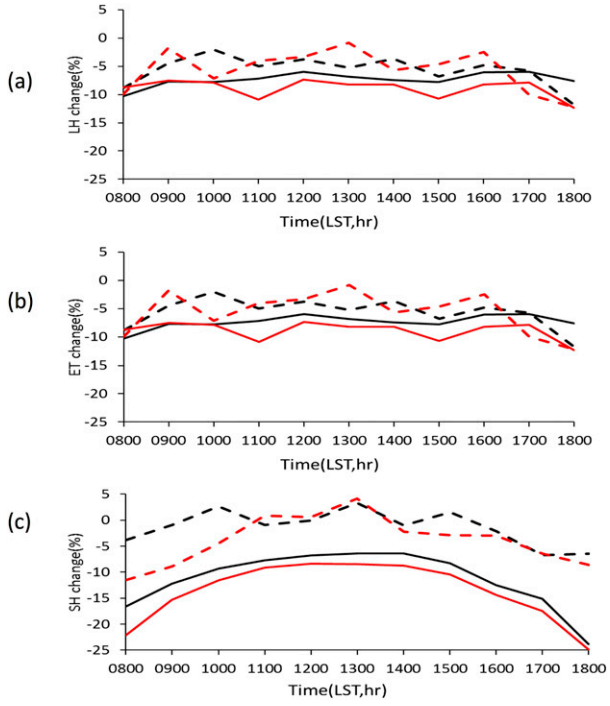

FIG. 11. Differences of (a) surface LH, (b) evapotranspiration, and (c) surface SH between P_ALL and C_ALL (black) and between P_ALL and P_NORAD (red) at the plain (solid line) and Mt. Hua top area (dashed line). The definitions of the plain and Mt. Hua top areas are as in Fig. 10.

summer of 2008 by employing the improved chemistry version of the Weather Research and Forecasting Model (WRF-Chem v3.4.1) with the MOSAIC sectional aerosol model. Sensitivity tests with reduced anthropogenic emissions (i.e., the clean condition) and removing aerosol–radiation interaction are conducted to examine how anthropogenic pollution in the Guanzhong Plain impacts precipitation in the downwind Mt. Hua region. We find that anthropogenic pollution in the upwind plain reduces the precipitation in the Mt. Hua region by up to 40% and the reduction mainly occurs in the daytime through aerosol–radiation interaction for summer convective clouds.

Further analyses of the mechanism for aerosol–radiation interaction suggest that the major reduction during the analysis period is through its impact on the cloud systems controlled by valley–mountain circulation, which is associated with the most frequent type of precipitation events, and a mesoscale cold-front event. Here, we present the mechanism revealed by model simulations that leads to the reduced mountainous precipitation through aerosol–radiation interaction for valley breeze–driven precipitation events consistent with the observed daytime precipitation reduction. That is, the strong absorbing properties of aerosols in the valley reduce the temperature differences between the valley and mountain at the elevated altitudes and cool the valley surface evidently, both of which lead to a weakened valley breeze at the daytime. The weakened valley breeze circulation and the reduced water vapor in the valley due to reduced evapotranspiration as a result of surface cooling dramatically reduce the transport of water vapor from the valley to mountain as well as the RH over the mountain, resulting in much weakened convection and reduced precipitation by suppressing convection intensity and therefore the ice-precipitating hydrometeor production.

This study provides a potential mechanism that could partially explain the long-term decreasing trend of precipitation observed in Mt. Hua and other mountainous areas in eastern China as air pollution increases in the recent decades (Yang et al. 2013a,b; Yang and Gong 2010). Observational data analysis reported in previous studies also showed the decreasing trend of wind speed for wind blowing from the valley to mountain, supporting the mechanism presented here. This study shows how aerosols change the local circulation and impact precipitation significantly through aerosol–radiation interaction for the cases when valley–mountain circulation dominates under relatively weak large-scale and synoptic forcing. Under the condition of strong absorbing polluted conditions, the local circulation change induced by the aerosol radiative effect controls convection and warm-season precipitation. The mechanism presented in the study may be applicable to other mountain areas with orographic precipitation mainly controlled by valley and mountain breezes. For cases with large-scale and synoptic forcing such as in the mesoscale cold-front event on 4 July 2008, the mechanisms for explaining the dramatic reduction of precipitation over Mt. Hua is totally different and reflects rather complicated changes in the large-scale circulation. The detailed analysis will be presented in a follow-on paper.

We hypothesize that how aerosols in the upwind plain area change precipitation over the mountainous region downwind can be dependent on many factors such as geographic locations, topographic features, aerosol properties, and meteorological conditions. Combining with the recent study of Fan et al. (2015), we show that, at the two locations of China, aerosols modify orographic precipitation in an opposite way but through the same aerosol–radiation interactions. At the Longmen Mountain that rises up to the Tibetan Plateau and downwind of a large plain—Sichuan basin (Fan et al. 2015)—we find that ARI significantly enhances rainfall intensity in the mountain during a flood event with ample moisture supply from upwind regions through ''aerosol-enhanced conditional instability.'' That is, aerosols suppress convection by absorbing solar radiation and increasing atmospheric

Brought to you by NOAA Central Library | Unauthenticated | Downloaded 08/13/24 01:21 PM UTC

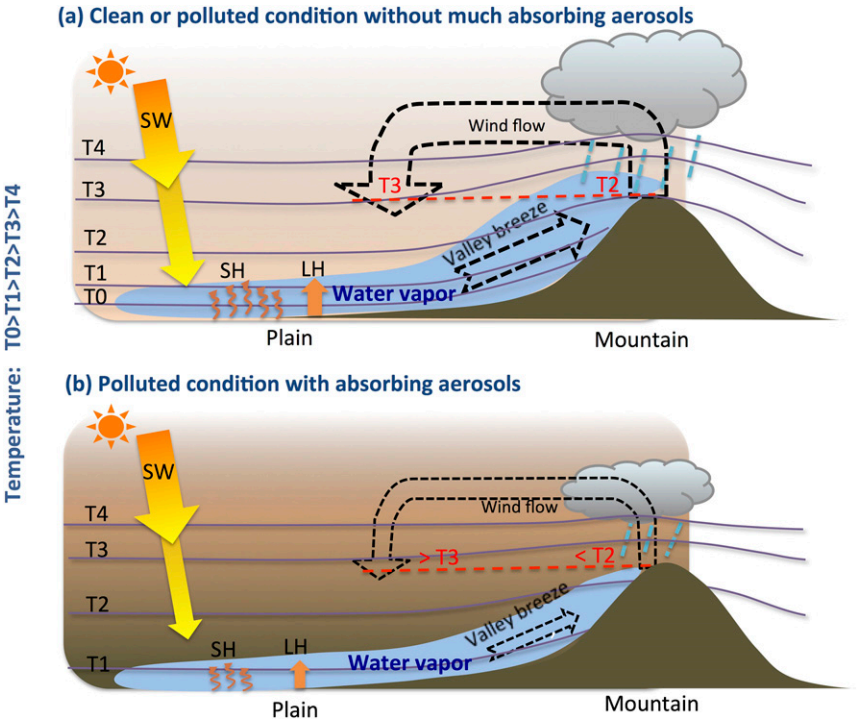

FIG. 12. Illustration of the mechanism for the weakened valley breeze in the polluted environment (a) with weak aerosol absorption compared with (b) the environment with strong absorption. Because of strong absorbing properties of aerosols in the polluted condition as shown in (b), the temperature is increased at the elevated layer over the valley and reduced at the surface of the mountaintop area compared with (a). Therefore, the temperature differences between the valley and mountain at the altitudes of the mountain peak are reduced [cf. the red dashed line in (b) with that in (a)]. In addition, aerosols in the polluted environment strongly cool the surface temperature in the valley, which weakens the rising motion. Both the reduced temperature differences in the elevated levels and the surface cooling weaken the valley breeze, significantly reducing the transport of water vapor from the valley to mountain. Along with the reduced water vapor near the surface of the valley due to reduced LH as a result of surface cooling, water vapor and RH over the mountaintop area are dramatically reduced, leading to much weakened convection and precipitation.

stability in the large basin during daytime, which allows excess moist air to be transported to the mountainous areas in the evening and orographically lifted to produce much stronger convection and heavier precipitation (Fan et al. 2015).

Aerosol indirect effect (i.e., ACI) might be playing some role in reducing precipitation as suggested in Rosenfeld et al. (2007) and Rosenfeld and Givati (2006). Since two-moment bulk schemes have limitations in representing aerosol indirect effects—for example, saturation adjustment approach for condensation (Wang et al. 2013) and separate size sorting for the number and mass mixing ratios of a hydrometeor (Milbrandt and Yau 2005)—our results on ACI might have large uncertainty.

Acknowledgments. This study was supported by the U.S. Department of Energy (DOE) Office of Science Biological and Environmental Research as part of the Regional and Global Climate Modeling program (RGCM) and the Ministry of Science and Technology (2013CB955804). The Pacific Northwest National Laboratory (PNNL) is operated for the DOE by Battelle Memorial Institute under Contract DE-AC06-76RLO1830. ZI is also supported by DOE (DESC0007171), NOAA (NA15NWS4680011), and NSF (AGS1534670). The model simulations were performed using PNNL Institutional Computing. The model and observational data can be obtained by contacting Jiwen.Fan@pnnl.gov.

REFERENCES

Altaratz, O., I. Koren, L. A. Remer, and E. Hirsch, 2014: Review: Cloud invigoration by aerosols—Coupling between microphysics and dynamics. *Atmos. Res.*, **140–141**, 38–60, doi:10.1016/j.atmosres.2014.01.009.

Brought to you by NOAA Central Library | Unauthenticated | Downloaded 08/13/24 01:21 PM UTC

Arakawa, A., and C.-M. Wu, 2013: A unified representation of deep moist convection in numerical modeling of the atmosphere. Part I. *J. Atmos. Sci.*, **70**, 1977–1992, doi:10.1175/JAS-D-12-0330.1.

Ault, A. P., C. R. Williams, A. B. White, P. J. Neiman, J. M. Creamean, C. J. Gaston, F. M. Ralph, and K. A. Prather, 2011: Detection of Asian dust in California orographic precipitation. *J. Geophys. Res.*, **116**, D16205, doi:10.1029/2010JD015351.

Bennartz, R., J. Fan, J. Rausch, L. R. Leung, and A. K. Heidinger, 2011: Pollution from China increases cloud droplet number, suppresses rain over the East China Sea. *Geophys. Res. Lett.*, **38**, L09704, doi:10.1029/2011GL047235.

Bollasina, M. A., Y. Ming, and V. Ramaswamy, 2011: Anthropogenic aerosols and the weakening of the South Asian summer monsoon. *Science*, **334**, 502–505, doi:10.1126/science.1204994.

——, ——, and ——, 2013: Earlier onset of the Indian monsoon in the late twentieth century: The role of anthropogenic aerosols. *Geophys. Res. Lett.*, **40**, 3715–3720, doi:10.1002/grl.50719.

Bond, T. C., and Coauthors, 2013: Bounding the role of black carbon in the climate system: A scientific assessment. *J. Geophys. Res. Atmos.*, **118**, 5380–5552, doi:10.1002/jgrd.50171.

Chen, F., and J. Dudhia, 2001: Coupling an advanced land surface–hydrology model with the Penn State–NCAR MM5 modeling system. Part I: Model implementation and sensitivity. *Mon. Wea. Rev.*, **129**, 569–585, doi:10.1175/1520-0493(2001)129<0569:CAALSH>2.0.CO;2.

Creamean, J. M., and Coauthors, 2013: Dust and biological aerosols from the Sahara and Asia influence precipitation in the western U.S. *Science*, **339**, 1572–1578, doi:10.1126/science.1227279.

Dentener, F., and Coauthors, 2006: Emissions of primary aerosol and precursor gases in the years 2000 and 1750 prescribed data-sets for AeroCom. *Atmos. Chem. Phys.*, **6**, 4321–4344, doi:10.5194/acp-6-4321-2006.

Fan, J., R. Zhang, W.-K. Tao, and K. I. Mohr, 2008: Effects of aerosol optical properties on deep convective clouds and radiative forcing. *J. Geophys. Res.*, **113**, D08209, doi:10.1029/2007JD009257.

——, D. Rosenfeld, Y. Ding, L. R. Leung, and Z. Li, 2012: Potential aerosol indirect effects on atmospheric circulation and radiative forcing through deep convection. *Geophys. Res. Lett.*, **39**, L09806, doi:10.1029/2012GL051851.

——, L. R. Leung, D. Rosenfeld, Q. Chen, Z. Li, J. Zhang, and H. Yan, 2013: Microphysical effects determine macrophysical response for aerosol impacts on deep convective clouds. *Proc. Natl. Acad. Sci. USA*, **110**, E4581–E4590, doi:10.1073/pnas.1316830110.

——, and Coauthors, 2014: Aerosol impacts on California winter clouds and precipitation during CalWater 2011: Local pollution versus long-range transported dust. *Atmos. Chem. Phys.*, **14**, 81–101, doi:10.5194/acp-14-81-2014.

——, D. Rosenfeld, Y. Yang, C. Zhao, L. R. Leung, and Z. Li, 2015: Substantial contribution of anthropogenic air pollution to catastrophic floods in southwest China. *Geophys. Res. Lett.*, **42**, 6066–6075, doi:10.1002/2015GL064479.

Fast, J., W. I. Gustafson Jr., R. C. Easter, R. A. Zaveri, J. C. Barnard, E. G. Chapman, G. A. Grell, and S. E. Peckham, 2006: Evolution of ozone, particulates, and aerosol direct radiative forcing in the vicinity of Houston using a fully coupled meteorology–chemistry–aerosol model. *J. Geophys. Res.*, **111**, D21305, doi:10.1029/2005JD006721.

Ginoux, P., M. Chin, I. Tegen, J. M. Prospero, B. Holben, O. Dubovik, and S. J. Lin, 2001: Sources and distributions of dust aerosols simulated with the GOCART model. *J. Geophys. Res.*, **106**, 20 255–20 273, doi:10.1029/2000JD000053.

Givati, A., and D. Rosenfeld, 2004: Quantifying precipitation suppression due to air pollution. *J. Appl. Meteor.*, **43**, 1038–1056, doi:10.1175/1520-0450(2004)043<1038:QPSDTA>2.0.CO;2.

Grant, L. D., and S. C. van den Heever, 2014: Microphysical and dynamical characteristics of low-precipitation and classic supercells. *J. Atmos. Sci.*, **71**, 2604–2624, doi:10.1175/JAS-D-13-0261.1.

Guo, J., M. Deng, J. Fan, Z. Li, Q. Chen, P. Zhai, Z. Dai, and X. Li, 2014: Precipitation and air pollution at mountain and plain stations in northern China: Insights gained from observations and modeling. *J. Geophys. Res. Atmos.*, **119**, 4793–4807, doi:10.1002/2013JD021161.

Hong, S.-Y., Y. Noh, and J. Dudhia, 2006: A new vertical diffusion package with an explicit treatment of entrainment processes. *Mon. Wea. Rev.*, **134**, 2318–2341, doi:10.1175/MWR3199.1.

Iacono, M. J., J. S. Delamere, E. J. Mlawer, M. W. Shephard, S. A. Clough, and W. D. Collins, 2008: Radiative forcing by long-lived greenhouse gases: Calculations with the AER radiative transfer models. *J. Geophys. Res.*, **113**, D13103, doi:10.1029/2008JD009944.

IPCC, 2013: *Climate Change 2013: The Physical Science Basis*. Cambridge University Press, 1535 pp, doi:10.1017/CBO9781107415324.

Jirak, I. L., and W. R. Cotton, 2006: Effect of air pollution on precipitation along the front range of the Rocky Mountains. *J. Appl. Meteor. Climatol.*, **45**, 236–245, doi:10.1175/JAM2328.1.

Khain, A. P., D. Rosenfeld, and A. Pokrovsky, 2005: Aerosol impact on the dynamics and microphysics of deep convective clouds. *Quart. J. Roy. Meteor. Soc.*, **131**, 2639–2663, doi:10.1256/qj.04.62.

Kok, J. F., 2011: A scaling theory for the size distribution of emitted dust aerosols suggests climate models underestimate the size of the global dust cycle. *Proc. Natl. Acad. Sci. USA*, **108**, 1016–1021, doi:10.1073/pnas.1014798108.

Lau, K.-M., and K.-M. Kim, 2006: Observational relationships between aerosol and Asian monsoon rainfall, and circulation. *Geophys. Res. Lett.*, **33**, L21810, doi:10.1029/2006GL027546.

Lee, D., Y. C. Sud, L. Oreopoulos, K.-M. Kim, W. K. Lau, and I.-S. Kang, 2014: Modeling the influences of aerosols on pre-monsoon circulation and rainfall over Southeast Asia. *Atmos. Chem. Phys.*, **14**, 6853–6866, doi:10.5194/acp-14-6853-2014.

Lee, K. H., Z. Li, M. S. Wong, J. Xin, Y. Wang, W.-M. Hao, and F. Zhao, 2007: Aerosol single scattering albedo estimated across China from a combination of ground and satellite measurements. *J. Geophys. Res.*, **112**, D22S15, doi:10.1029/2007JD009077.

Levin, Z., and W. R. Cotton, 2009: *Aerosol Pollution Impact on Precipitation: A Scientific Review*. Springer, 386 pp., doi:10.1007/978-1-4020-8690-8.

Liu, Y.-C., J. Fan, G. J. Zhang, K.-M. Xu, and S. J. Ghan, 2015: Improving representation of convective transport for scale-aware parameterization: 2. Analysis of cloud-resolving model simulations. *J. Geophys. Res. Atmos.*, **120**, 3510–3532, doi:10.1002/2014JD022145.

Lynn, B., A. Khain, D. Rosenfeld, and W. L. Woodley, 2007: Effects of aerosols on precipitation from orographic clouds. *J. Geophys. Res.*, **112**, D10225, doi:10.1029/2006JD007537.

Milbrandt, J. A., and M. K. Yau, 2005: A multimoment bulk microphysics parameterization. Part I: Analysis of the role of the spectral shape parameter. *J. Atmos. Sci.*, **62**, 3051–3064, doi:10.1175/JAS3534.1.

Brought to you by NOAA Central Library | Unauthenticated | Downloaded 08/13/24 01:21 PM UTC

Morrison, H., and W. W. Grabowski, 2012: Large-scale thermodynamic and dynamic controls on aerosol-induced invigoration of tropical deep convection. *Geophysical Research Abstracts*, Vol. 14, Abstract EGU2012-6449. [Available online at http://meetingorganizer.copernicus.org/EGU2012/EGU2012-6449.pdf.]

——, J. A. Curry, and V. I. Khvorostyanov, 2005: A new double-moment microphysics parameterization for application in cloud and climate models. Part I: Description. *J. Atmos. Sci.*, **62**, 1665–1677, doi:10.1175/JAS3446.1.

Muhlbauer, A., and U. Lohmann, 2008: Sensitivity studies of the role of aerosols in warm-phase orographic precipitation in different dynamical flow regimes. *J. Atmos. Sci.*, **65**, 2522–2542, doi:10.1175/2007JAS2492.1.

——, and ——, 2009: Sensitivity studies of aerosol–cloud interactions in mixed-phase orographic precipitation. *J. Atmos. Sci.*, **66**, 2517–2538, doi:10.1175/2009JAS3001.1.

Rosenfeld, D., and A. Givati, 2006: Evidence of orographic precipitation suppression by air pollution–induced aerosols in the western United States. *J. Appl. Meteor. Climatol.*, **45**, 893–911, doi:10.1175/JAM2380.1.

——, J. Dai, X. Yu, Z. Yao, X. Xu, X. Yang, and C. Du, 2007: Inverse relations between amounts of air pollution and orographic precipitation. *Science*, **315**, 1396–1398, doi:10.1126/science.1137949.

——, and Coauthors, 2008: Flood or drought: How do aerosols affect precipitation? *Science*, **321**, 1309–1313, doi:10.1126/science.1160606.

Saleeby, S. M., W. R. Cotton, D. Lowenthal, R. D. Borys, and M. A. Wetzel, 2009: Influence of cloud condensation nuclei on orographic snowfall. *J. Appl. Meteor. Climatol.*, **48**, 903–922, doi:10.1175/2008JAMC1989.1.

——, ——, ——, and J. Messina, 2013: Aerosol impacts on the microphysical growth processes of orographic snowfall. *J. Appl. Meteor. Climatol.*, **52**, 834–852, doi:10.1175/JAMC-D-12-0193.1.

Tao, W.-K., X. Li, A. Khain, T. Matsui, S. Lang, and J. Simpson, 2007: Role of atmospheric aerosol concentration on deep convective precipitation: Cloud-resolving model simulations. *J. Geophys. Res.*, **112**, D24S18, doi:10.1029/2007JD008728.

——, J.-P. Chen, Z. Li, C. Wang, and C. Zhang, 2012: Impact of aerosols on convective clouds and precipitation. *Rev. Geophys.*, **50**, RG2001, doi:10.1029/2011RG000369.

Twomey, S., 1977: The influence of pollution on the shortwave albedo of clouds. *J. Atmos. Sci.*, **34**, 1149–1152, doi:10.1175/1520-0469(1977)034<1149:TIOPOT>2.0.CO;2.

van den Heever, S. C., G. G. Carrió, W. R. Cotton, P. J. DeMott, and A. J. Prenni, 2006: Impact of nucleating aerosol on Florida storms. Part I: Mesoscale simulations. *J. Atmos. Sci.*, **63**, 1752–1775, doi:10.1175/JAS3713.1.

van der Werf, G. R., and Coauthors, 2010: Global fire emissions and the contribution of deforestation, savanna, forest, agricultural, and peat fires (1997–2009). *Atmos. Chem. Phys.*, **10**, 11 707–11 735, doi:10.5194/acp-10-11707-2010.

Wang, C., 2005: A modeling study of the response of tropical deep convection to the increase of cloud condensation nuclei concentration: 1. Dynamics and microphysics. *J. Geophys. Res.*, **110**, D21211, doi:10.1029/2004JD005720.

Wang, Y., J. Fan, R. Zhang, L. R. Leung, and C. Franklin, 2013: Improving bulk microphysics parameterizations in simulations of aerosol effects. *J. Geophys. Res. Atmos.*, **118**, 5361–5379, doi:10.1002/jgrd.50432.

Xiao, H., Y. Yin, L. Jin, Q. Chen, and J. Chen, 2014: Simulation of aerosol effects on orographic clouds and precipitation using WRF Model with a detailed bin microphysics scheme. *Atmos. Sci. Lett.*, **15**, 134–139, doi:10.1002/asl2.480.

Yang, J., and D.-Y. Gong, 2010: Intensified reduction in summertime light rainfall over mountains compared with plains in eastern China. *Climatic Change*, **100**, 807–815, doi:10.1007/s10584-010-9863-0.

Yang, X., M. Ferrat, and Z. Li, 2013a: New evidence of orographic precipitation suppression by aerosols in central China. *Meteor. Atmos. Phys.*, **119**, 17–29, doi:10.1007/s00703-012-0221-9.

——, Z. Yao, Z. Li, and T. Fan, 2013b: Heavy air pollution suppresses summer thunderstorms in central China. *J. Atmos. Sol.-Terr. Phys.*, **95–96**, 28–40, doi:10.1016/j.jastp.2012.12.023.

Zaveri, R. A., and L. K. Peters, 1999: A new lumped structure photochemical mechanism for large-scale applications. *J. Geophys. Res.*, **104**, 30 387–30 415, doi:10.1029/1999JD900876.

——, R. C. Easter, J. D. Fast, and L. K. Peters, 2008: Model for Simulating Aerosol Interactions and Chemistry (MOSAIC). *J. Geophys. Res.*, **113**, D13204, doi:10.1029/2007JD008782.

Zhang, H., Z. Wang, P. Guo, and Z. Wang, 2009a: A modeling study of the effects of direct radiative forcing due to carbonaceous aerosol on the climate in East Asia. *Adv. Atmos. Sci.*, **26**, 57–66, doi:10.1007/s00376-009-0057-5.

Zhang, Q., and Coauthors, 2009b: Asian emissions in 2006 for the NASA INTEX-B mission. *Atmos. Chem. Phys.*, **9**, 5131–5153, doi:10.5194/acp-9-5131-2009.

Zhao, C., X. Liu, L. R. Leung, B. Johnson, S. A. McFarlane, W. I. Gustafson Jr., J. D. Fast, and R. Easter, 2010: The spatial distribution of mineral dust and its shortwave radiative forcing over North Africa: Modeling sensitivities to dust emissions and aerosol size treatments. *Atmos. Chem. Phys.*, **10**, 8821–8838, doi:10.5194/acp-10-8821-2010.

——, L. Ruby Leung, R. Easter, J. Hand, and J. Avise, 2013a: Characterization of speciated aerosol direct radiative forcing over California. *J. Geophys. Res. Atmos.*, **118**, 2372–2388, doi:10.1029/2012JD018364.

——, S. Chen, L. R. Leung, Y. Qian, J. F. Kok, R. A. Zaveri, and J. Huang, 2013b: Uncertainty in modeling dust mass balance and radiative forcing from size parameterization. *Atmos. Chem. Phys.*, **13**, 10 733–10 753, doi:10.5194/acp-13-10733-2013.

Zubler, E. M., L. Ulrike, L. Daniel, S. Christoph, and M. Andreas, 2011: Statistical analysis of aerosol effects on simulated mixed-phase clouds and precipitation in the Alps. *J. Atmos. Sci.*, **68**, 1474–1492, doi:10.1175/2011JAS3632.1.

Brought to you by NOAA Central Library | Unauthenticated | Downloaded 08/13/24 01:21 PM UTC